Article

Enhancing the strength and ductility of a medium entropy alloy through non-basal slip activation

Zhen Chen[1,7], Yang Chen[1,2,7], Daixiu Wei[1,2], Xu Liu [1], Xuan Luo[3], Henggao Xiang[1], Wu Gong[4], Stefanus Harjo [4], Takuro Kawasaki [4], Rui Hou[1], Jinpeng Zhang[1], Demin Zhu[1], Jiheng Tang[1], Luo Li[1], Jianghui Xie[1], Gong Zheng[1], Zhixiang Qi[1], Howard Sheng [5,6] ✉ & Guang Chen [1] ✉

Developing alloys with both ultrahigh strength and ductility remains a formidable scientific challenge, primarily due to the inherent strength-ductility tradeoff. Here, we present an approach to enhance the ductility and strength of a medium-entropy alloy (MEA) featuring a fully recrystallized face-centered cubic/hexagonal close-packed dual-phase ultrafine-grained architecture. This is achieved by activating unusual non-basal slips in the ordered hexagonal close-packed superlattice nanoprecipitates, resulting in this MEA that exhibits remarkable uniform elongation (ε_u) and ultrahigh yield strength (σ_y) across a wide temperature range, particularly at cryogenic temperatures (σ_y ~ 2100 MPa, ε_u ~ 15%). The non-basal slips in the secondary phase are activated at ultrahigh stress levels, which are compatible with the increased yield strength of the MEA attained through multiple strengthening mechanisms, including grain boundaries, lattice friction, and second-phase nanoprecipitates provided by the multi-principal elements of the entropy alloy. The deformation mechanism elucidated in this work not only leverages the significant strengthening and strain hardening effects of brittle nanoprecipitates but also enables the ductilization of the alloy through sequential non-basal slip during ongoing deformation.

High-performance bulk metallic materials with ultrahigh σ_y and excellent ε_u are highly desirable for developing reliable, energy-efficient, and light-weight components across automotive, aircraft, and airspace industries. For most metallic materials, however, an increase in strength often comes at the expense of ductility, displaying the strength-ductility trade-off[1,2]. Hence, in traditional simple alloy systems, only a few martensite-based steels could occasionally accomplish the goal[3,4]. Unfortunately, such ultrahigh-strength steels usually lose most of their toughness and ductility when the temperature falls below the ductile-brittle transition temperature, limiting their further applications at cryogenic temperatures[5].

The recent emergence of high- or medium-entropy alloys (H/MEAs), employing multiple-principal-element systems, opens a new avenue to break through the strength-ductility paradox[6,7]. Unlike simple metals, these alloys exhibit appreciable concentration inhomogeneity[8], local chemical order[9,10], and severe lattice distortion[11],

[1]Jiangsu Belight Laboratory, State Key Laboratory of Advanced Casting Technologies, Nanjing University of Science and Technology, Nanjing 210094, China. [2]State Key Laboratory of Light Superalloys, Luoyang 471023, China. [3]Key Laboratory for Light-weight Materials, Nanjing Tech University, Nanjing, China. [4]J-PARC Center, Japan Atomic Energy Agency, Tokai-mura, Naka-gun, Ibaraki 319-1195, Japan. [5]Center for High Pressure Science and Technology Advanced Research, Shanghai, China. [6]Department of Physics and Astronomy, George Mason University, Fairfax, VA, USA. [7]These authors contributed equally: Zhen Chen, Yang Chen. ✉e-mail: hsheng@gmu.edu; gchen@njust.edu.cn

which can result in unusual dislocation behaviors and unprecedented mechanical properties[9–11]. Superior strength and ductility, high strain hardening, and exceptional damage tolerance have been realized in some single-phase face-centered cubic (fcc) alloys[6,7,11]. Nonetheless, these fcc H/MEAs, have a relatively low σ_y[7], limiting their potential usability.

An effective approach for enhancing σ_y is the introduction of ordered intermetallic compounds (IMCs) into the matrix, known as the second phase strengthening[12]. However, most IMCs with atomically ordered structure are intrinsically brittle, causing local stress concentration and triggering premature fracture[12]. To date, only a few simple ductile IMCs with high-symmetry cubic crystal structure, such as B2 and L1$_2$-type ordered phases, have been successfully introduced into multicomponent fcc solid-solutions to improve mechanical properties[13–16]. These multiple-phase H/MEAs usually evolve from several ternary or quaternary derivatives of the Cantor alloy[6] via further alloying with elements like Ti and Al, leading to rather limited freedom for compositional adjustments. Additionally, certain B2-type IMCs-strengthened H/MEAs suffer from reduced ductility at cryogenic temperatures[17–19]. Consequently, the development of effective IMCs for second-phase strengthening in fcc H/MEAs has encountered a bottleneck, and other structurally simple IMCs need to be further exploited to enhance the strength-ductility synergy.

Traditionally, the D0$_{19}$ phase (e.g., Ti$_3$Al, Co$_3$W, and Ni$_3$Sn), one of the simplest ordered hexagonal close-packed (hcp) superlattices, is considered to be a highly favorable strengthening phase[20–22]. For example, α_2-Ti$_3$Al with a D0$_{19}$ superlattice structure is a significant constituent phase in the TiAl-based alloys[20]. However, polycrystalline aggregates of D0$_{19}$-type IMCs exhibit limited ductility and toughness at room temperature and below due to the difficulty in activating pyramidal slip of dislocations with a Burgers vector of $<2c + a>$, which is required to accommodate strain along the c-axis of the D0$_{19}$ unit cell[23,24]. The difficulty in generating these non-basal dislocations lies primarily in their high critical activating stresses[24].

Here, we address this dilemma by demonstrating that non-basal slip activated in a material strengthened by a D0$_{19}$ IMC precipitate can provide both strength and ductility. We illustrate this in a NiCoCr$_{0.5}$V$_{0.5}$ MEA using tensile tests over a wide temperature range spanning from room temperature to liquid-helium temperature. We have observed the unexpected non-basal slip of D0$_{19}$ IMCs during the deformation of a duplex phase UFG structure. This dual-phase UFG architecture comprises a fully recrystallized fcc UFG matrix and D0$_{19}$ nano-lamellae. The combination of grain-boundary strengthening from the fcc UFG matrix and solid solution strengthening from the multi-principal elements in the fcc matrix, generates sufficiently high matrix stress levels to overcome the stress barrier for pyramidal slip of D0$_{19}$ nano-lamellae. This approach demonstrates that by achieving sufficiently high matrix stress levels, brittle D0$_{19}$ nano-precipitates can be transformed into a ductile strengthening phase without initiating damage at the heterointerfaces. Coupled with the formation of dynamically refined nanosized dislocation and stacking fault (SF) substructures in the fcc UFG matrix, our duplex phase UFG alloy exhibits promising mechanical properties over a broad temperature range, particularly achieving a σ_y of ~2100 MPa and a ε_u of ~15% at cryogenic temperatures.

Results and discussion

The as-cast alloy underwent homogenization at 1150 °C, followed by hot forging, and was then cold-rolled to 1.5 mm-thick sheets with 96% total thickness reduction (CR state). X-ray diffraction (XRD) results confirmed that the CR sample remains in a single fcc phase (Supplementary Fig. 1a). Transmission electron microscopy (TEM) observations verified that the cold deformed microstructure consists of extremely refined nanosized grains with a high density of dislocations and SFs, without elemental segregation (Supplementary Fig. 2). An annealing treatment was then performed at 750 °C for 15 min (hereinafter referred to as CR750) to obtain the fcc/D0$_{19}$ duplex phase UFG architecture (Supplementary Fig. 1). After annealing, a uniformly recrystallized microstructure developed featuring nano-scale D0$_{19}$ lamellae embedded in the fcc UFG matrix. The fcc UFG matrix (mean grain size: 409 nm; 75.8 vol%) exhibited an equiaxed grain morphology with abundant annealing twins, as illustrated by transmission Kikuchi diffraction (TKD) results (Fig. 1a–c). The nanoscale D0$_{19}$ lamellae
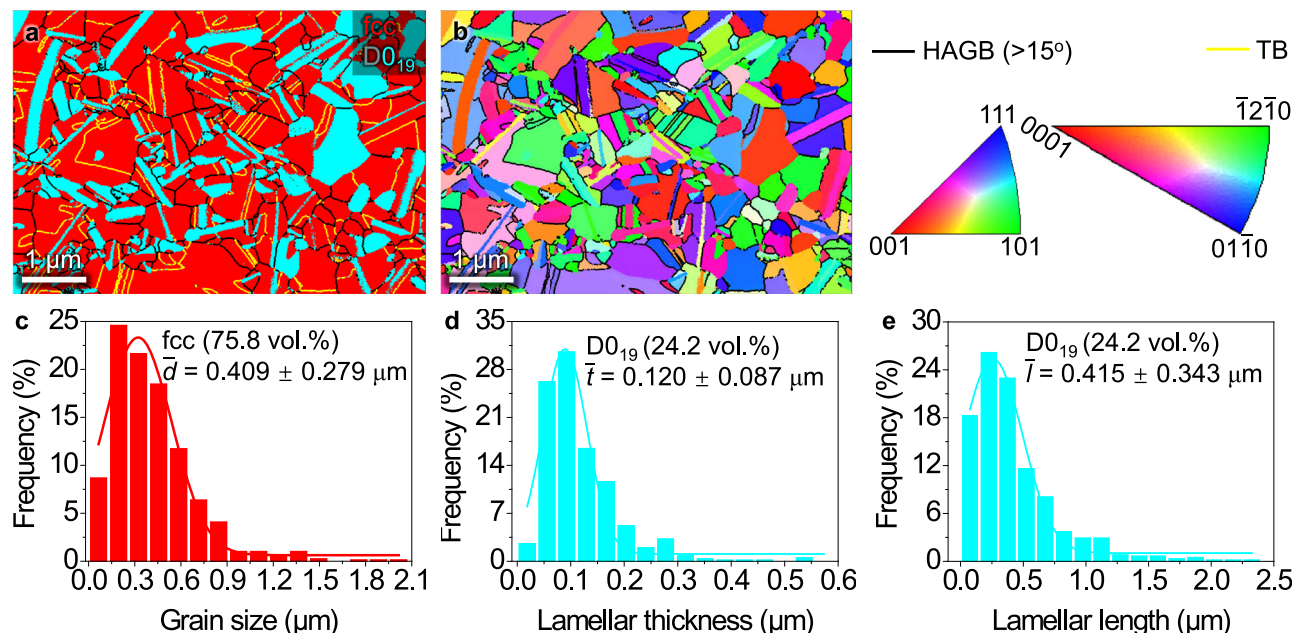

Fig. 1 | Transmission Kikuchi diffraction (TKD) characterization for the CR750 alloy, showing a fully-recrystallized fcc/D0$_{19}$ (fcc/D0$_{19}$) dual-phase ultrafine-grained (UFG) architecture. a TKD phase map. **b** TKD inverse pole figure. **c–e** Statistical size distribution of (**c**) grain size of the fcc UFG matrix, (**d**) D0$_{19}$ lamellar thickness, and (**e**) D0$_{19}$ lamellar length. 'HAGB' and 'TB' denote high-angle grain boundary and twin boundary, respectively. TKD measurements were repeated three times on three distinct samples to enable statistical size analysis. The combined dataset was used for size distribution analysis and fitted with Gaussian functions (solid lines), revealing approximately normal distributions. Source data for (**c–e**) are provided as a Source data file.
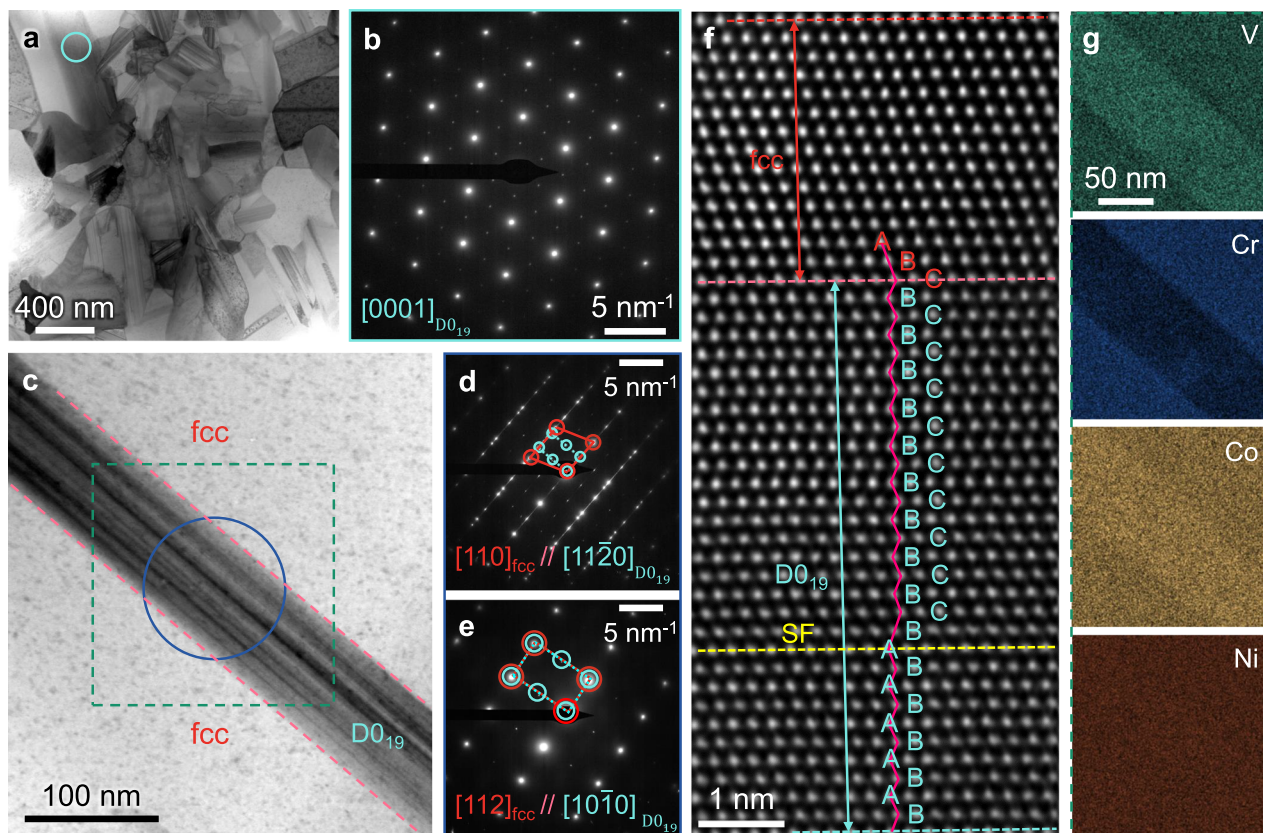
Fig. 2 | Scanning transmission electron microscopy (STEM) characterization for the CR750 alloy. a, c STEM-BF images viewed from different directions. **b** Corresponding selected area electron diffraction (SAED) pattern from the cyan circle in (**a**). **d, e** Corresponding SAED patterns from the blue circle in (**c**). Red and cyan circles represent diffraction signals from the fcc matrix and the $D0_{19}$ phase,

respectively. **f** Atomic-scale STEM high angle annular dark-field (STEM-HAADF) image of the fcc/$D0_{19}$ dual-phase region, showing $D0_{19}$ lamellae decorated with a high density of stacking faults. **g** Corresponding STEM energy-dispersive X-ray spectroscopy (STEM-EDS) mapping from the green square in (**c**), showing elemental partitioning in the two phases.

(mean thickness: 120 nm; aspect ratio: 3.5; 24.2 vol%) frequently intersected to form interconnected colonies that spanned the entire fcc grain (Fig.1a, b, d, e). TEM characterization further revealed that the $D0_{19}$ superlattice structure is perfectly coherent with the fcc matrix (Fig. 2). Scanning TEM bright-field (STEM-BF) images near the $[11\bar{2}0]$ zone axis and the STEM high-angle annular dark-field (STEM-HAADF) atomic lattice image showed that the $D0_{19}$ phase contains smaller substructures, decorated with massive SFs (Fig. 2c, d, f). Specific crystallographic orientation relationships were also observed between the fcc matrix and the $D0_{19}$ lamellae: $\{1\bar{1}1\}_{fcc}$ // $\{0002\}_{D0_{19}}$ and $<110>_{fcc}$ // $<11\bar{2}0>_{D0_{19}}$; $\{220\}_{fcc}$ // $\{\bar{2}4\bar{2}0\}_{D0_{19}}$ and $<\bar{1}12>_{fcc}$ // $<10\bar{1}0>_{D0_{19}}$; $\{13\bar{1}\}_{fcc}$ // $\{\bar{2}4\bar{2}2\}_{D0_{19}}$ and $<112>_{fcc}$ // $<10\bar{1}0>_{D0_{19}}$ (Fig. 2c–e). An obvious elemental partitioning between the duplex phases existed with V atoms segregating into $D0_{19}$ lamellae and Cr atoms enriching in fcc matrix (Fig. 2g). Neutron diffraction (ND) measurements further confirmed that the lattice parameter at 298 K $a = 0.3578$ nm for the fcc matrix, and $a = 0.5051$ nm and $c = 0.4112$ nm for the $D0_{19}$ lamellae (Supplementary Fig. 1b).

We performed three-dimensional atom probe tomography (3D-APT) to offer a quantitative compositional analysis for the CR750 alloy at the atomic scale. The 3D-APT results revealed a clear elemental partitioning between the fcc and $D0_{19}$ duplex phases, with V-rich regions corresponding to the $D0_{19}$ lamellae and Cr atoms segregating into the fcc matrix (Fig. 3a), in excellent accordance with the STEM-EDS mapping result (Fig. 2g). A one-dimensional compositional profile shows the quantitative elemental partitioning of each element (Fig. 3b), with the chemical composition of $Ni_{31.99}Co_{34.47}Cr_{18.52}V_{15.02}$ (at.%) in the fcc matrix and $Ni_{34.67}Co_{35.08}Cr_{11.50}V_{18.75}$ (at.%) in the $D0_{19}$

lamellae. We identified the $D0_{19}$ IMC as the Ni_3Sn-type ordered superlattice[22], with Ni, Co, and Cr atoms occupying the 'Ni' sites, and V atoms substituting for the 'Sn' sublattice. The atomic arrangements of the superlattice are schematically shown in Fig. 3c, d. We evaluated the energetics of several competing models, including disordered-hcp, $D0_{19}$-ordered, and $D0_a$-ordered structures based on density-functional theory (DFT) calculations (Supplementary Table 1). The $D0_{19}$ configuration exhibited the lowest formation energy (-5.354 eV atom^{-1}), confirming its thermodynamic stability as an ordered superlattice. Furthermore, single-crystal electron diffraction simulations, based on the established $D0_{19}$-ordered superlattice (Supplementary Fig. 3), particularly the extra weak spots due to the superlattices, showed good agreement with our TEM analyses (Fig. 2b, d, e), verifying the existence of the $D0_{19}$ phase. Detailed crystallographic information of this $D0_{19}$ structure is provided in Supplementary Table 2. Our subsequent molecular dynamics (MD) simulations of the mechanical properties of the $D0_{19}$ phase were based on the as-constructed atomistic model.

The CR750 alloy exhibits impressive tensile properties, combining an ultrahigh σ_y of 1575 MPa and a large ε_u of 10.1% at ambient temperature (298 K) (Fig. 4a, Supplementary Fig. 4 and Supplementary Table 3). As the temperature decreases, both the strength and ductility further enhance simultaneously. Specifically, σ_y and ε_u rise to 2095 MPa and 15.0% at liquid-nitrogen temperature (77 K), and 2146 MPa and 15.5 % at liquid-helium temperature (4.2 K), respectively. Repeated tests of different samples exhibited highly consistent results (Supplementary Fig. 4a). This is a remarkable outcome for ultrahigh-strength bulk alloys, demonstrating superb strength-ductility synergy
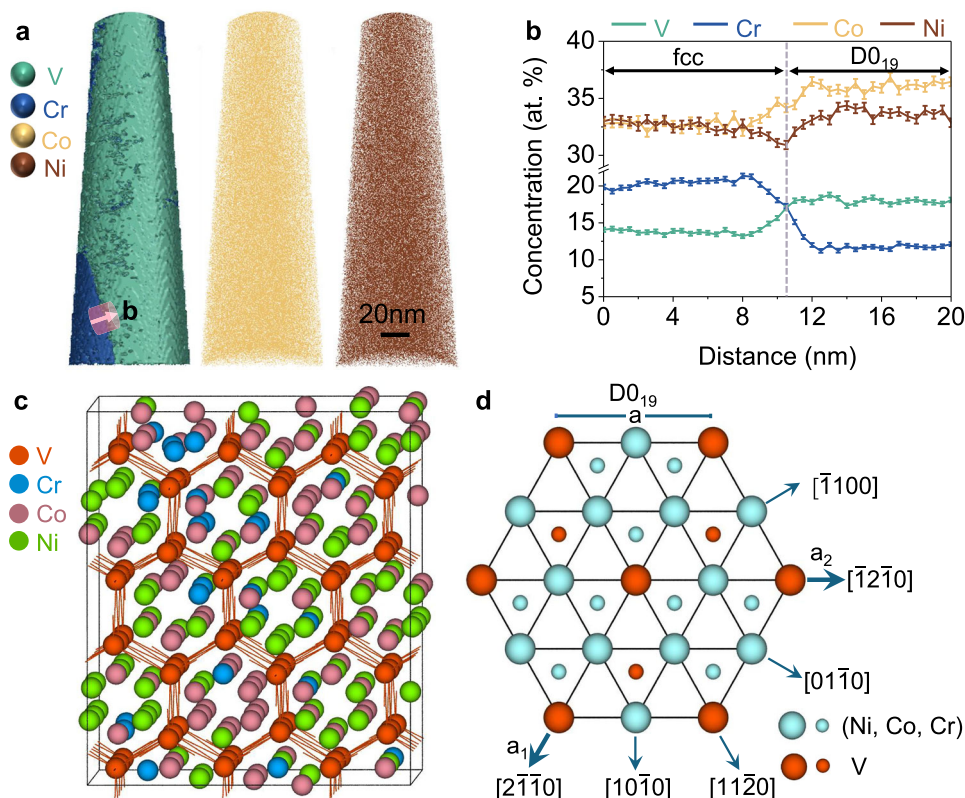
Fig. 3 | Three-dimensional compositional distributions of the dual-phase fcc/D0$_{19}$ UFG architecture in the CR750 alloy. a Three-dimensional reconstruction map of a typical atom probe tomography tip showing the distribution of each element. The fcc/D0$_{19}$ interface is highlighted using iso-composition surfaces containing 18 at.% V and 18 at.% Cr. **b** one-dimensional compositional profiles computed along the white arrow in (**a**), showing the compositional changes across the interface. Error bars refer to the standard deviations of the counting statistics in each bin of the profiles. Standard error s is calculated as: $s = \sqrt{\frac{c_i(1-c_i)}{n_t}}$ in which n_t is

the total number of ions in the sample, and c_i is the concentration in atomic fraction of solute i in the sample, which is calculated as: $c_i = \frac{n_i}{n_t}$ in which n_i is the number of ions of solute i in the sample. **c** Ordered crystallographic structure and site occupancies of the D0$_{19}$ phase viewed along the c-axis direction by density functional theory calculations. **d** Atomic arrangement in the (0001) planes of the D0$_{19}$ phase with a (Ni, Co, Cr)$_3$V stoichiometry. Large circles represent atoms in the A-layer, the plane of the paper, and small circles represent atoms in the B-layer, immediately below the A-layer. Source data for (**b**) are provided as a Source data file.

over a wide temperature range. The strength-ductility combinations can even compete with those of some ultrahigh-strength steels, which typically suffer from inhomogeneous plastic flow[3,4] and ductile-to-brittle transition[5]. Interestingly, even at such an ultrahigh σ_y in the post-yield region, the present alloy shows exceptional strain-hardening rates, which increase as the temperature decreases (Fig. 4b). This contributes to delaying plastic instability while maintaining excellent ε_u. We compared the tensile properties of the CR750 alloy with other high-performance bulk alloys[15,17,19,25–61] (Fig. 4c, d, Supplementary Fig. 4b and Supplementary Table 4). Our alloy stands out in terms of σ_y vs ε_u, over a wide temperature range from 298 K to 4.2 K.

The ultrahigh σ_y of the CR750 alloy primarily derives from grain boundary strengthening, lattice friction stress from the fcc UFG matrix, and second-phase strengthening from the D0$_{19}$ lamellae. In the CR750 alloy, the ordered D0$_{19}$ lamellae are stronger than the disordered fcc UFG matrix, as demonstrated by our nano-indentation tests (Supplementary Fig. 5). Consequently, the fcc/D0$_{19}$ phase boundaries act as effective barriers against dislocation motion. Based on Hall-Petch relation modeling of the fcc matrix and the rule of mixtures[62], we quantified the strengthening contributions of the fcc grain boundaries (787 MPa at 298 K and 1069 MPa at 77 K), the lattice friction (167 MPa at 298 K and 315 MPa at 77 K), and the D0$_{19}$ lamellae (621 MPa at 298 K and 711 MPa at 77 K) (Supplementary Fig. 6).

To uncover the origin of the high strain-hardening capability of the CR750 alloy at ultrahigh stress levels, we performed TKD

experiments for the tension-fractured samples at 298 K, 77 K, and 4.2 K, respectively. Our observation revealed that as the deformation temperature decreases, the CR750 alloy deforms more homogeneously (Supplementary Fig. 7), indicating an increasingly significant role played by the D0$_{19}$ lamellae in carrying plasticity at low temperatures. Inhomogeneous plastic deformation features at phase interfaces, grain boundaries, twinning boundaries, and within grain interiors of the fcc UFG matrix are clearly visible at 298 K, significantly reduced at 77 K, and become almost undiscernible at 4.2 K (Supplementary Fig. 7). Neither mechanical twins nor deformation induced transformation were detected during straining at any temperatures (Supplementary Fig. 7).

To elucidate the underlying deformation mechanism, detailed TEM analyses were conducted on the CR750 alloy samples strained at various temperatures. At 298 K, dislocation planar slip dominates in the fcc UFG matrix across the entire strain range, forming a directionally nanosized dislocation substructure with increasing strain (spacing ≈ 66 nm) (Supplementary Fig. 8a, d, g). Additionally, the D0$_{19}$ lamellae demonstrate a significant capability to accommodate deformation. At low-to-medium strains, <a>-type dislocations of the D0$_{19}$ superlattice were observed and their quantities increased with increasing strain (Supplementary Fig. 8b, c, e, f). It is worth noting that prolific non-basal <$2c+a$>-type dislocations (pyramidal slip) appeared at the late stage of deformation after tensile fracture (Supplementary Fig. 8h, i).

At 77 K, at a strain of ~2% (Fig. 5a), dislocation slip is activated on the {111} planes in the fcc UFG matrix, accompanied by the appearance
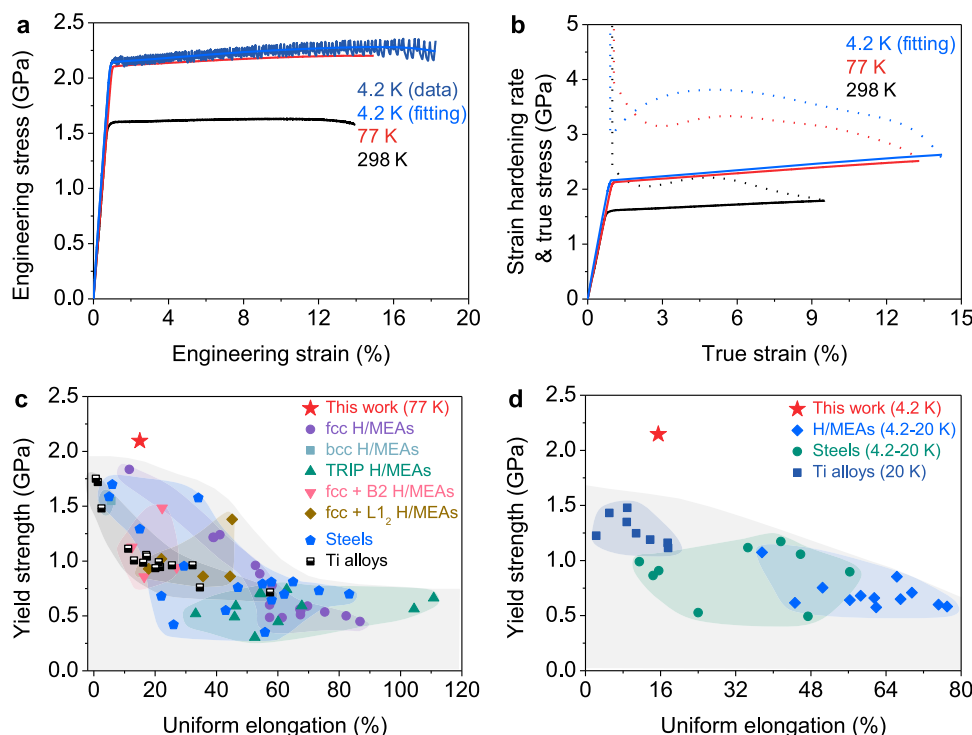
Fig. 4 | Tensile properties of the CR750 alloy and comparison with other high-performance alloys. a Engineering stress-strain curve tested at 298 K (black line), 77 K (red line), and 4.2 K (blue lines), respectively. **b** Corresponding strain-hardening rate (dotted lines) and true stress (solid lines) vs true strain curves. Due to the strong serrations observed in the 4.2 K tensile tests, we performed polynomial fitting on the engineering stress-strain curve to determine the strain-hardening rate. **c**, **d** Comparison of the CR750 against other state-of-the-art alloys in terms of their σ_y vs ε_u at 77 K (**c**) and 4.2–20 K (**d**), respectively. The data on the mechanical properties of these reported materials are also listed in Supplementary Table 4. This work has a superior combination of σ_y and ε_u compared with other alloys, including fcc H/MEAs[25–36], body-centered cubic (bcc) H/MEAs[37], TRIP H/MEAs[38–42], fcc + B2 H/MEAs[17,19,43,44], fcc + L1$_2$ H/MEAs[15,45–47], steels[29,48–53], H/MEAs[26,27,29,30,32,34–36,54], and Ti alloys[55–61]. 'H/MEAs' and 'TRIP' denote high/medium entropy alloys and transformation-induced plasticity. Source data are provided as a Source data file.

of a few SFs, indicating the early stage of planar dislocation glide. As the strain increases to ~5% (Fig. 5d), a much higher density of SFs is generated, and intersecting SFs commence. Upon reaching fracture strain (Fig. 5g), hierarchical SF networks with nanoscale spacing (~34 nm) become activated, accompanied by the formation of Lomer−Cottrell (LC) locks (Fig. 6a). Highlighting the deformation responses of the DO$_{19}$ lamellae, we show that, unlike at 298 K, <c> and <2c + a >-type dislocations are successively activated at 77 K even at small strains and persist through the entire strain range. The number of various types of dislocations stored in the DO$_{19}$ lamellae is significantly higher than those at 298 K (Fig. 5b, c, e, f, h, i). Additionally, some <2c + a> dislocations, e.g., dislocation 1 and 2 in Fig. 5e, h, exhibit step-shaped configurations, indicating that the <2c + a> dislocations may undergo double cross-slips between the first-order (pyramidal I) and the second-order (pyramidal II) pyramidal slip systems, further enabling a compatible and continuous deformation[63].

The deformation characteristics of the CR750 alloy after tensile fracture at 4.2 K shows similar deformation substructures to those at 77 K (Supplementary Fig. 9). The notable differences include a much denser SF network (with a spacing of ≈10 nm) in the fcc UFG matrix and a much higher dislocation density in the DO$_{19}$ lamellae. These deformation features indicate that the role of the DO$_{19}$ lamellae in accommodating deformation is further enhanced by the easier generation of non-basal dislocations. The abundance of SFs coupled with the formation of LC locks after cryogenic deformation at 4.2 K is likely responsible for the observed serrated flow at ultralow temperatures[27,64]. In addition, we observed that certain dislocations can transmit across the phase boundaries from the fcc matrix into the DO$_{19}$ lamellae during straining (Fig. 5 and Supplementary Figs. 8 and 9).

To gain insights into the evolution of crystal defects in real-time, we conducted in situ ND measurements on the CR750 alloy at 298 K and 77 K. During tensile deformation, the diffraction peaks of the fcc/DO$_{19}$ duplex phases show progressive broadening and shifts with increasing strain, indicating the continuous accumulation of defects such as dislocations and SFs (Supplementary Fig. 10a, b). Also, the CR750 maintained a fcc/DO$_{19}$ dual-phase state throughout tensile straining, with no phase transformation observed (Supplementary Fig. 10c). The derived SF probability (SFP) at 77 K was much higher than at 298 K (Fig. 6a), consistent with our TEM results (Fig. 5 and Supplementary Fig. 8). Convolutional multiple whole profile (CMWP) analysis of the ND data also revealed a significantly higher density of dislocation at 77 K, compared to 298 K (Fig. 6b). While quantitative analysis of crystal defects in the DO$_{19}$ lamellae during tensile deformation would be of great interest, the low diffraction peak intensity renders such analysis intractable.

Based on the observations outlined above, we explore the physical origin of the excellent tensile ductility of the CR750 alloy. Typically, the deformation mechanism of the fcc-based metals is governed by the SF energy (SFE), which dictates the deformation mode: single dislocation glide for SFE above 45 mJ/m^2, mechanical twinning for SFE between 15 and 45 mJ/m^2, and deformation-induced phase transformation for SFE below 15 mJ/m^2 (ref.[65].). We have quantified the SFEs of the fcc matrix through weak-beam dark-field STEM analysis (Supplementary Figs. 11 and 12), finding values of 24 ± 4 mJ/m^2 at 298 K and 18 ± 2 mJ/m^2 at 77 K, respectively, which aligns satisfactorily with our theoretical calculations of the SFE without considering the temperature effect (Supplementary Table 5). Given that the SFE values fall within the range of 15−45 mJ/m^2, mechanical twins are therefore
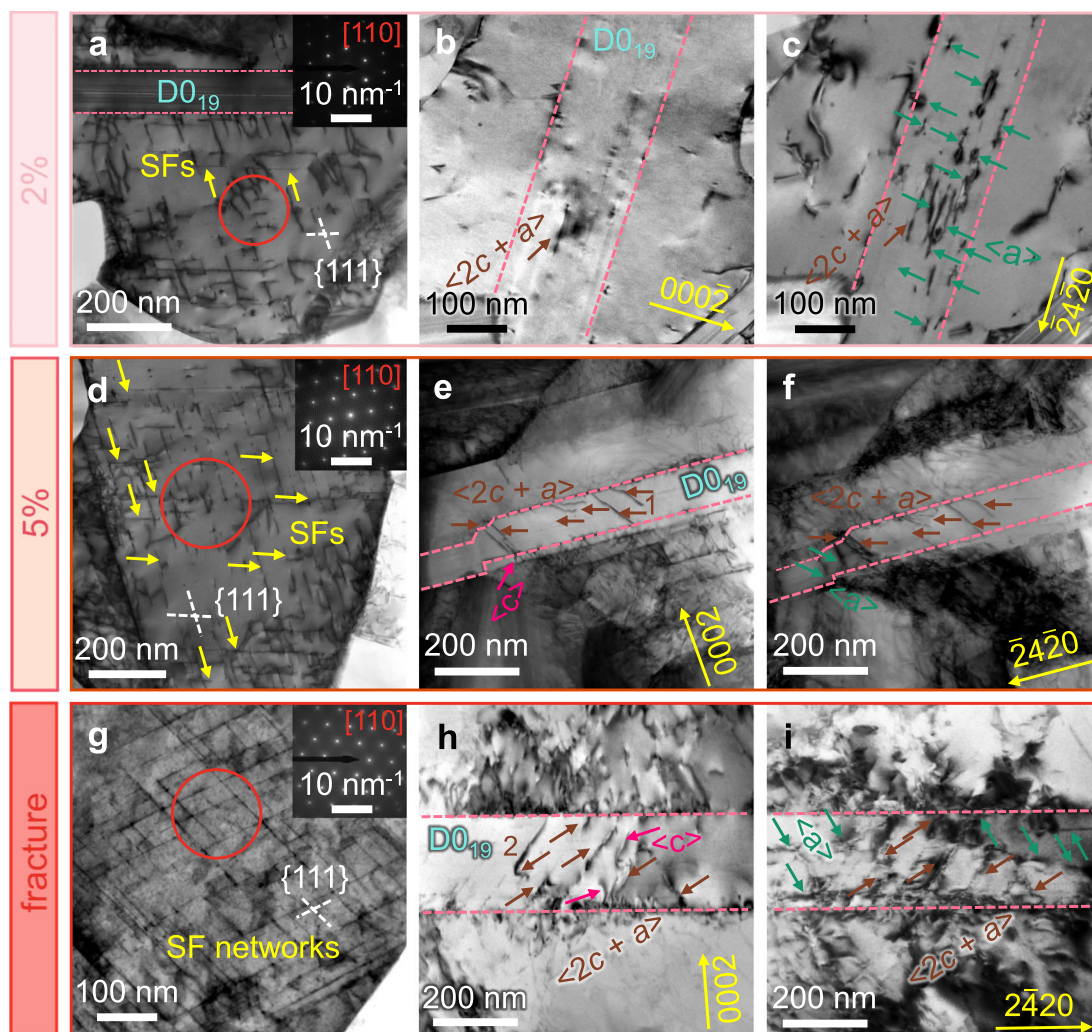
Fig. 5 | Deformation mechanism of the CR750 alloy at 77 K. a STEM-BF image of the 2% strain, showing the early stage of planar slip, accompanied by the occurrence of a small number of stacking faults (SFs) in the fcc UFG matrix; the inset shows the corresponding SAED pattern from the region outlined by the red circle. **b, c** Two-beam STEM-BF images of the $D0_{19}$ phase after 2% strain, with the viewing direction of [10$\bar{1}$0] under **g** = [000$\bar{2}$] (**b**) and **g** = [$\bar{2}$4$\bar{2}$0] (**c**), respectively. **d** STEM-BF image of the 5% strain, showing the formation of a high density of SFs in the fcc UFG matrix; the inset shows the corresponding SAED pattern from the region outlined by the red circle. **e, f** Two-beam STEM-BF images of the $D0_{19}$ phase after 5% strain, with the viewing direction of [10$\bar{1}$0] under **g** = [0002] (**e**) and **g** = [$\bar{2}$4$\bar{2}$0] (**f**), respectively. **g** STEM-BF image of the fracture sample that shows the formation of nano-spaced hierarchical SF networks in the fcc UFG matrix; the inset shows the corresponding SAED pattern from the region outlined by the red circle. **h, i** Two-beam STEM-BF images of the $D0_{19}$ phase after fracture, with the viewing direction of [10$\bar{1}$0] under **g** = [0002] (**h**) and **g** = [$\bar{2}$4$\bar{2}$0] (**i**), respectively.

expected to be the underlying deformation mechanisms. However, the fcc UFG matrix and coherently nanosized $D0_{19}$ lamellae significantly impede the initiation of mechanical twins[15,16,66]. As a result, dynamically refined SFs are preferred during the plastic deformation due to their relatively low critical stress[15,16]. Therefore, planar-slip predominates in the plastic deformation of the fcc UFG matrix at 298 K due to relatively low flow stress, while SFs become the dominant mechanism at cryogenic temperatures, facilitated by further enhanced flow stress and reduced SFE.

The compositionally disordered fcc matrix maintains a coherent interface with the structurally ordered $D0_{19}$ phase, allowing transmission of dislocations across heterointerfaces with minimal resistance[67]. Specifically, the activation of these <c>-component dislocations (i.e., either <c> or <2c + a>-type dislocations) enhances transmission of edge dislocations in fcc UFG matrix across phase boundaries[68], avoiding dislocation jam and relieving stress concentration. Nevertheless, as these non-basal dislocations are activated relatively late at 298 K, their contribution to plasticity is limited. Consequently, the notable strain hardening rate at 298 K is primarily due to the dynamic

slip-band refinement in the fcc UFG matrix. The accumulation of massive dislocations within the slip bands significantly reduces the mean free path of the mobile dislocations, which increasingly hinders their movement as the strain increases and the slip-band spacing narrows. Moreover, pronounced slip planarity curtails dynamic recovery and promotes dislocation storage[11], leading to a high and sustained strain-hardening rate and extensive uniform elongation at 298 K.

At cryogenic temperatures, the substantially increased stress enables the early generation of non-basal dislocations after yielding, thus greatly improving the deformability of the $D0_{19}$ lamellae. The deformation behavior helps mitigate stress concentration at the phase boundaries, prevents premature crack initiation, and leads to uniform macroscopic plastic deformation. Furthermore, the hierarchical SF networks dynamically subdivide the fcc UFG matrix into even finer nano-domains during straining, reducing their mean free path of dislocations and increasing the strain-hardening capability through a dynamic Hall-Petch effect[15,16]. Besides, the formation of the numerous immobile LC locks not only acts as a strong obstacle to pin the
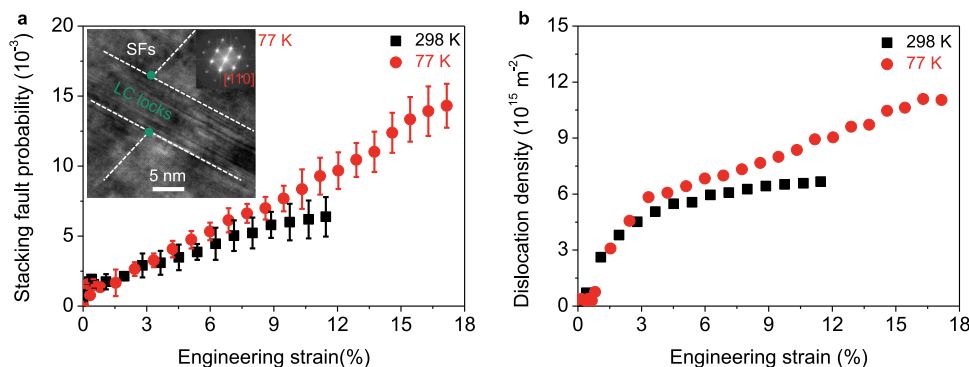
Fig. 6 | Crystal defect evolutions during straining in the CR750 alloy measured by in-situ neutron diffraction. a SF probability (SFP) vs engineering strain in the fcc UFG matrix at 77 K (red solid circles), with the result at 298 K (black solid squares) plotted together for comparison. The inset shows a high-resolution TEM image of the intersected SF networks with the LC locks in the fcc UFG matrix after fracture. The error bars are conveyed from errors of peak fit of neutron diffraction profiles, since the SFP is calculated from peak center variations. **b** Dislocation density vs engineering strain in the fcc UFG matrix at 77 K (red solid circles), with the result at 298 K (black solid squares) plotted together for comparison. Source data are provided as a Source data file.

dislocation motion, but also promotes the dislocation multiplication by serving as Frank-Read dislocation sources, thereby facilitating consistent and progressive strain-hardening rates[15,16]. As such, the synergies of the dual-phase UFG architecture with the coherent boundaries, dynamically refined SF networks, high-density immobile LC locks, and extensive activation of the non-basal dislocations in DO_{19} lamellae collectively enhance the plastic deformation stability and strain-hardening capability of the CR750 alloy at cryogenic temperatures, resulting in the superior tensile ductility at an ultrahigh-strength level.

We now elucidate the possibility of non-basal slips within the DO_{19} lamellae. The likelihood of activating non-basal dislocations (e.g., pyramidal dislocations) in the DO_{19} phase is intrinsically linked to the critical resolved stress (CRSS) of their slip systems, Schmid factors, and the external loads. To reveal the dislocation plasticity, we computed the generalized stacking fault energies (GSFEs) that govern dislocation activation and pathways, along with the CRSS of the corresponding slip systems at 298 K (Fig. 7, Supplementary Figs. 13 and 14, and Supplementary Tables 5 and 6), combining both large-scale MD and DFT. These computations reveal that, as a result of superdislocation activation, the CRSS for pyramidal I slip systems reaches up to 800 MPa, and for pyramidal II, it escalates to 875 MPa at 298 K, which is roughly one order of magnitude higher than that of the bulk fcc matrix phase (105 MPa).

The corresponding Schmid factors for these pyramidal systems in our experiments are provided in Supplementary Fig. 15, with pyramidal I exhibiting the largest Schmid factors with a mean value of 0.437, closely followed by pyramidal II at 0.392. Considering the CRSS values and Schmid factors, we estimated the corresponding average normal stress (NS) for the activation of these slip systems at 298 K (Supplementary Fig. 16). Specifically, the NS values of two pyramidal slip systems (1831 MPa for pyramidal I and 2232 MPa for pyramidal II) are larger than the flow stress at the onset of yielding, indicating that the activation of the $<2c + a>$ dislocations is difficult during the initial deformation stage at 298 K, aligning well with our experimental observations. As strains increase, strain hardening from the dynamically refined slip bands in the fcc matrix and $<a>$ dislocation slips within DO_{19} lamellae enable the resolved shear stress (RSS) acting on the pyramidal slip systems with high Schmid factors to surpass the CRSS at higher strains, signaling the engagement of $<2c + a>$ dislocations during the later stages of deformation, moderately extending its plasticity.

In contrast, as temperatures drop to 77 K and below, the flow stress values increase rapidly to reach ~2100 MPa at yielding (Fig. 4).

This increase enables $<2c + a>$ dislocations to activate at the early stages of deformation. Meanwhile, the enhanced defect proliferation efficiency at cryogenic temperatures boosts the flow stress, further augmenting the non-basal slipping capability of the DO_{19} lamellae. The facilitation of non-basal slip essentially results from an extremely high dislocation glide stress in the fcc matrix caused by the UFG and the high solution friction stress (Supplementary Figs. 6 and 13 and Supplementary Table 6). As deformation progresses and flow stress increases, more $<2c + a>$ dislocations are sequentially activated with the RSS surpassing the CRSS required for the non-basal slipping. Consequently, such non-basal slip in the DO_{19} lamellae, together with the multiple strain hardening mechanisms within the fcc UFG matrix, imparts unparalleled strength and ductility to this alloy at cryogenic temperatures.

The dual-phase UFG architecture of our $NiCoCr_{0.5}V_{0.5}$ MEA, featuring high-density DO_{19}-type nano-scale lamellae within the complex alloy system, confers attractive ductility and ultrahigh strength at ambient and cryogenic temperatures. Beyond the dynamically refined nano-sized dislocation or SF substructures, the CR750 alloy utilizes the deformability of the DO_{19} superlattice through the sufficient activation of non-basal dislocations, substantially enhancing the alloy's overall ductility. We anticipate that the microstructural design concept holds promise for broad applications across various other alloy systems, including TiAl-based alloys, superalloys, and H/MEAs, potentially delivering exceptional properties for critical applications.

Methods

Materials preparation
Bulk $NiCoCr_{1-X}V_X$ (χ = 0.4, 0.5, 0.6, at.%) MEA ingots were prepared by magnetic levitation melting of high-purity constituent metals (>99.9 wt%) under a high-purity argon atmosphere. The as-cast ingots (60 mm in height × 90 mm in diameter) were homogenized at 1150 °C for 2 h under argon, followed by hot forging into billets (240 mm (length) × 40 mm (width) × 40 mm (height)). Subsequent thermo-mechanical processing included cold rolling to 1.5 mm thickness (96% reduction) and annealing at 700–850 °C for 10–15 min with water quenching.

To determine the Hall-Petch relationship and SFE of the fcc matrix, bulk ingots with composition $Ni_{31.99}Co_{34.47}Cr_{18.52}V_{15.02}$ (at.%)— matching the fcc UFG matrix in the CR750 alloy as identified by 3D-APT —were prepared via vacuum induction melting under argon atmosphere. The ingots were subjected to sequential thermo-mechanical processing: (i) homogenization at 1150 °C for 2 h, (ii) hot forging at 1150 °C, (iii) cold rolling with 85% thickness reduction, and (iv)
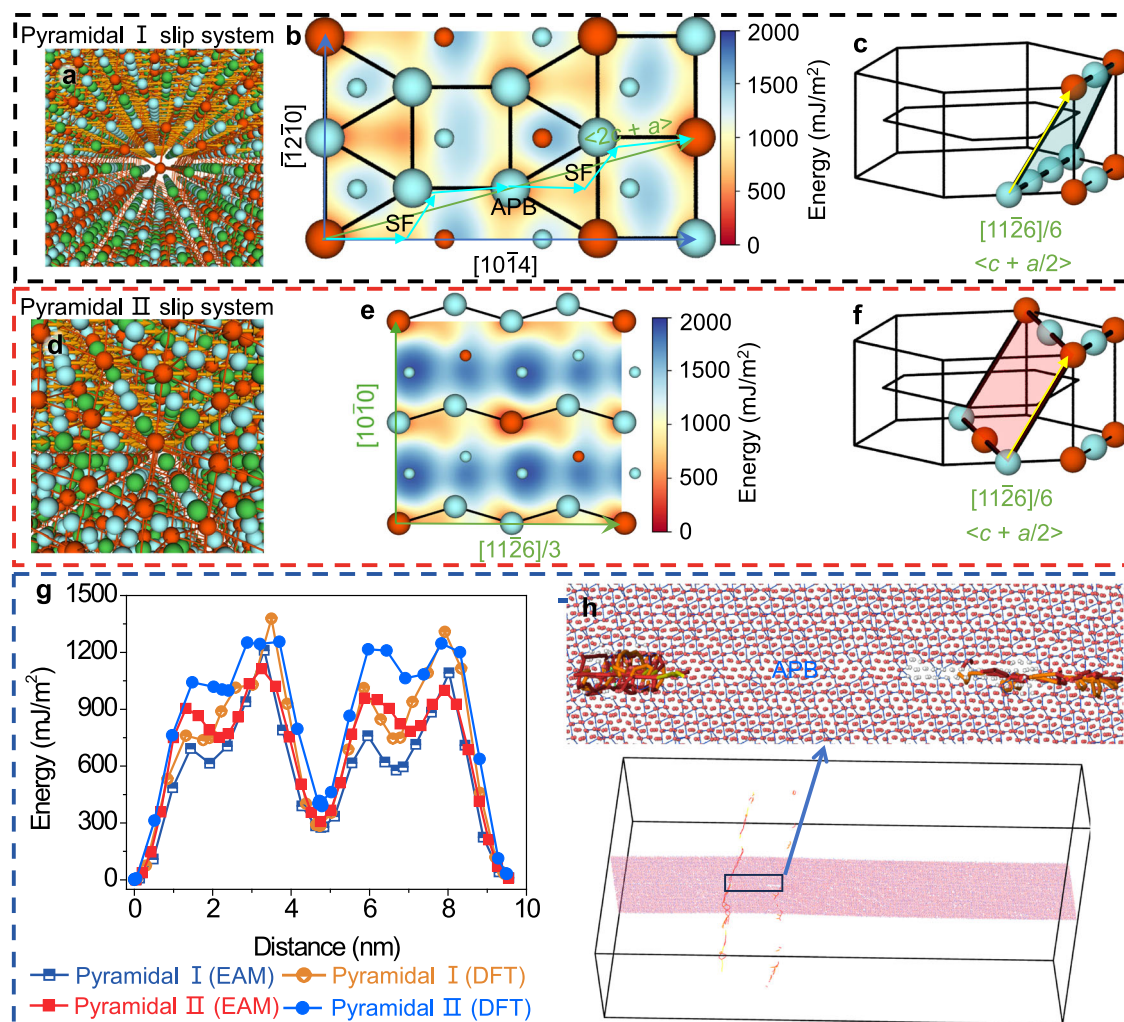
Fig. 7 | Generalized SF energies of the {2$\bar{2}$01} plane and {11$\bar{2}$1} plane in the D0$_{19}$ phase, and corresponding critical resolved shear stress (CRSS) calculation of their slip systems. a, d Atomic arrangements and slip directions in the pyramidal I (**a**), and pyramidal II (**d**) slip systems. **b, e** γ Surfaces of pyramidal I plane (**b**), and pyramidal II plane (**e**). The atomic packing scheme on each slip plane is overlaid on top of the γ surface. Note that the minimum energy path (MEP) for planar slip in the pyramid I slip system (**b**) is along the short arrows (cyan), rather than the long Burger's vector. **c, f** Illustration of slip systems in the D0$_{19}$ unit cell of pyramidal I plane (**c**), and pyramidal II plane (**f**) (not all atoms are shown). **g, h** MEPs of

pyramidal I plane (**g**), and pyramidal II plane (**h**) calculated by embedded atom method (EAM) and density functional theory (DFT). The slip paths are indicated by short arrows in (**b**) and (**e**), respectively. **i** CRSS calculation for pyramidal I slip system by molecular dynamics (MD). The <2c + a> superdislocation dissociates into superpartials and is separated by an antiphase boundary (APB) area, consistent with the MEP calculations and similar to ref. 89. Source data for (**g**) are provided as a Source data file. MD trajectory data and script for (**h**) are provided in the Supplementary Data.

recrystallization annealing at 850–1200 °C for varying durations under argon, followed by water quenching.

Mechanical properties at room temperature

Uniaxial quasi-static tensile tests were performed at room temperature (298 K) using an Instron 5980 testing machine at a constant strain rate of 1×10^{-3} s^{-1}. Dog-bone-shaped flat tensile specimens with gauge dimensions of $15 \times 3 \times 1.5$ mm^3 (length × width × thickness) were prepared by electrical discharge machining. Three repeat tests were conducted for statistical reliability, and strain measurements were acquired via a non-contact optical extensometer. Nanoindentation measurements were performed on the CR750 alloy using a Hysitron triboindenter equipped with a diamond Berkovich tip. A maximum load of 2000 μN was applied to characterize the hardness-depth profiles across different microstructural zones. To ensure statistical reliability, a 4×10 indentation matrix was implemented with 5 μm spacing between test points. Prior to testing, the sample was prepared by electrochemical polishing to achieve optimal surface conditions.

Tensile tests at cryogenic temperatures

Uniaxial tensile tests were performed on an Instron 5980 testing system at cryogenic temperatures of 77 K (liquid nitrogen) and 4.2 K (liquid helium), employing a constant strain rate of 1×10^{-3} s^{-1}. Specimens with dog-bone geometry were fabricated by electrical discharge machining, featuring gauge dimensions of $10 \times 2.5 \times 1.5$ mm^3 for 77 K tests and $27 \times 4 \times 1.5$ mm^3 for 4.2 K experiments. For cryogenic testing, specimens and fixtures were fully immersed in liquid nitrogen or liquid helium using two dedicated cryostats mounted on the testing machine's crosshead. To ensure statistical significance, four replicates were performed at 77 K and two at 4.2 K. Strain measurements were acquired using customized extensometers: an Epsilon 3442-010M-LT for 77 K measurements and an Epsilon 3542-025M-050-LT for 4.2 K characterization. In particular, the 4.2 K experiments utilized a vacuum-insulated cryogenic Dewar tank to minimize helium evaporation and maintain thermal stability. A rhodium-iron thermometer was installed in the cryogenic setup, positioned above the specimen to ensure accurate temperature monitoring at liquid helium levels.

SEM characterizations

The phase type, grain size, grain orientation, distribution, and phase fraction were characterized using the TKD technique performed with TESCAN CLARA plus Field Emission Gun SEM operating at 30 kV, equipped with the Oxford Instrument Channel 5 EBSD system and a Nordlys-S EBSD detector. The step size used for data collection was 10 nm. The TKD samples were prepared via electropolishing (Struers TenuPol-5 Twin Jet Electropolisher) in an electrolyte solution containing 10% perchloric acid and 90% alcohol at a temperature of −20 °C. TKD tests were repeated three times on three individual samples in order to perform a statistical size analysis, which involved counting 785 fcc grains and 619 $D0_{19}$ lamellae.

TEM characterizations

The microstructure of the recrystallized and pre-strained specimens was characterized by TEM, HRTEM, and STEM with a TALOS F200X G2 operating at 200 kV. An aberration-corrected Thermo Fisher Scientific Spectra300 was used to analyze the atomic-level STEM-HAADF image at an accelerating voltage of 300 kV. The observed specimens were first mechanically ground to 30 μm thickness and then twin-jet electropolished using 10% perchloric acid + 90% alcohol solution at a temperature of −20 °C.

To conduct the **g·b** analyses to determine the dislocation types activated in the $D0_{19}$ lamellae, we chose **g** = [0002] (or [000$\bar{2}$]) and **g** = [2$\bar{4}$20] (or [$\bar{2}$4$\bar{2}$0]) beams under the viewing direction of [10$\bar{1}$0] for STEM-BF imaging in the present work. **b** is the Burgers vector of the dislocation. Based on the **g·b** invisibility criterion, <2c + a> is simultaneously visible in the STEM-BF images obtained with **g** = [0002] (or [000$\bar{2}$]) and **g** = [2$\bar{4}$20] (or [$\bar{2}$4$\bar{2}$0]). <a> dislocation is invisible when **g** = [0002] (or [000$\bar{2}$]), and <c> dislocation is invisible when **g** = [2$\bar{4}$20] (or [$\bar{2}$4$\bar{2}$0]).

To quantitatively evaluate the SFEs of the fcc matrix in the CR750 alloy, TEM dislocation analysis was conducted on the recrystallized coarse-grained samples (composition: $Ni_{31.99}Co_{34.47}Cr_{18.52}V_{15.02}$) after 3% tensile deformation at 298 K (mean grain size: 26.3 μm) and 77 K (mean grain size: 44.3 μm), respectively. The separation behavior of partial dislocations was acquired by a **g**(3**g**) weak-beam dark-field STEM imaging method on a TALOS F200X G2 microscope. The **g·b** analysis of the partial dislocations (**g** = [02$\bar{2}$], **g** = [20$\bar{2}$], and **g** = [2$\bar{2}$0], respectively) was performed to identify the Burgers vectors, where the contrast from a dislocation is eliminated when **g·b** = 0. The actual partial dislocation separation was further obtained by calibrating the observed values, as proposed by Cockayne[69,70]. Then, the SFEs were estimated according to the following equation[69]:

$$SFE = \frac{Gb_p^2}{8\pi d_{act}}\left(\frac{2-\nu}{1-\nu}\right)1 - \left(\frac{2\nu\cos(2\beta)}{2-\nu}\right) \tag{1}$$

where G is the shear modulus of the fcc UFG matrix (85 GPa), b_p is the magnitude of the Burgers vector of partial dislocations (0.14612 nm at 298 K and 0.14588 nm at 77 K, respectively, derived from the measured lattice parameters based on ND patterns in Supplementary Figs. 1 and 10), d_{act} is the separation width of partial dislocations, ν is the Poisson ratio of the fcc UFG matrix (0.313), and β is the angle between the Burgers vector of perfect dislocation and the dislocation line. Note that the composition of the fcc UFG matrix is very close to that of $V_{0.4}Cr_{0.6}CoNi$ alloy, the values of G and ν are therefore adopted from this alloy[71].

APT characterizations

Needle-shaped APT specimens were prepared using Helios G4 UX dual-beam focused ion beam (FIB) tools with standard FIB lift-out procedures. APT experiments were performed using a local electrode atom probe (LEAP 4000× Si) with a specimen temperature of 40 K, a laser pulse repetition rate of 200 kHz, a laser pulse energy of 40 pJ, and a target evaporation of 0.8%. APT data analysis was performed using the CAMECA Visualization and Analysis Software (IVAS 3.8.6).

In situ ND measurements

To obtain the evolution of the planar defects probability and dislocation density during deformation, the samples before and after the tensile tests were characterized using a time-of-flight neutron diffractor at BL19 "TAKUMI" in the Materials and Life Science Facility (MLF) at the Japan Proton Accelerator Research Complex (J-PARC). The loading axis of the sample was oriented +45° to the incident neutron beam, and the width and height of the incident beam were set as 3 mm and 5 mm. The sample was mounted inside the cryogenic cell chamber, which was sealed and evacuated to <10^{-3} kPa before the cooling was started. A Gifford−McMahon (GM) cooler having a stage of 77 K was installed in the cryogenic load frame to cool the grips and the specimen. The sample was cooled down and held for 1 h at a stable temperature of 77 K (vacuum - 10^{-5} kPa) before the loading was commenced. Details of the instrument and measurement procedures for the ND have been reported in previous studies[72,73]. Continuous ND data were collected by two detector banks positioned at ±90° relative to the incident beam after an exposure time of 20 min, which corresponds to the loading and transverse directions of the specimen, respectively. The data at room temperature was also obtained in a similar manner. The collected diffraction profiles were analyzed using the Z-Rietveld code to calculate the lattice parameters, phase volume fraction, and {hkl}-dependent d-spacing of the individual phases[74,75].

The SFP was estimated from the difference in peak shifts between crystallographically equivalent orientations[74,75], i.e., {111}–{222} and {200}–{400} pairs, with the scattering vector parallel to the loading direction. The CMWP method, a modified Williamson-Hall method, was used to calculate the dislocation density[74–76]. The instrumental profile was acquired by measuring a LaB_6 standard powder sample under the same conditions for CMWP analysis. The experimental error margin was calculated by the fitting error.

The relative amounts of phases were calculated based on {200} γ-fcc and {20$\bar{2}$1} $D0_{19}$-hcp peaks using Sage and Guillaud's method described by Sage and Guillaud[77]:

$$f_{D0_{19}} = \frac{I_{D0_{19}}^{20\bar{2}1}}{I_{D0_{19}}^{20\bar{2}1} + 1.5 \times I_{fcc}^{200}} \tag{2}$$

where $f_{D0_{19}}$ is the fraction of $D0_{19}$ phase, and I is the integrated intensity of the corresponding ND peaks.

Ab initio calculations

All ab initio calculations were performed using the DFT-based Vienna Ab-initio Simulation Package (VASP). The projector augmented-wave (PAW) method[78,79] was used to describe the electron-ion interactions, and the generalized gradient approximation (GGA) was employed for exchange-correlation functionals. The valence electrons of Ni, Co, Cr, and V were specified as $3d^84s^2$, $3d^74s^2$, $3d^54s^2$, and $3d^34s^2$, respectively. The spin-polarization effect was not considered. For high-precision ab initio total-energy calculations, a K-spacing of 0.3 Å^{-1} was typically used. To calculate the formation energies of competing phases, the supercell method[10] was used with more than 300 atoms for each model. The formation energies were averaged over 20 configurations after geometric optimization.

Empirical interatomic potential development

An empirical potential for Ni−Co−Cr−V alloy system has been developed using the embedded atom method (EAM)[80–82], by matching a large ab initio database established for the quaternary system without explicit consideration of spin polarization. The ab initio database includes a comprehensive set of atomic configurations (see below)

with corresponding cohesive energies, atomic forces, and stress tensors. A similar force-matching method has previously been employed to develop highly optimized potentials for the ZrCuAl[82] and NiCoCr[10] systems. In this work, special attention was given to the energetics of various SFs and the ordering of Ni–Co–Cr–V solid solutions. To accurately model the Ni–Co–Cr–V system across its full compositional range, we increased the previous database established for the development of the Ni–Co–Cr potential. More than 7500 atomic configurations were selected to form a new ab initio database from non-spin-polarized DFT calculations. These atomic configurations encompass all reported IMCs in the Ni–Co–Cr–V system and include liquid/glass structures, various types of defects, transition pathways, and more, within a large pressure-temperature phase space. The revised Potfit code[81] was used for potential fitting. The potential was improved through an iterative process and further refined to match experimental data, including cohesive energies, lattice parameters, elastic constants, and phonon frequencies of the constituent elements. The as-developed EAM potential enables us to investigate the dislocation plasticity via large-scale MD.

Structural ordering in the MEA

The structural ordering and formation of the $D0_{19}$ phase from the Ni–Co–Cr–V MEA were investigated using hybrid MD/Monte Carlo (MC) simulations employing the EAM potential. First, we calculated the chemical potential of Co, Cr, V with respect to Ni employing hybrid MD and MC simulations under the semi-grand canonical ensemble at 1500 K, similar to ref. 10. The following chemical potentials were obtained for the $Ni_{0.333}Co_{0.333}Cr_{0.167}V_{0.167}$ composition: $\Delta\mu_{Ni-Cr} = -0.20$ eV, $\Delta\mu_{Ni-Co} = -0.13$ eV, and $\Delta\mu_{Ni-V} = -1.57$ eV. Subsequently, hybrid MD and MC simulations, with the variance-constrained semi-grand-canonical ensemble[83], were carried out to obtain the equilibrium configurations at different annealing temperatures T_a. The variance parameter κ used in our simulations is 10^3. The initial configuration consisted of 144,000 atomic sites with the x, y, and z directions aligned along the [11$\bar{2}$], [111], and [1$\bar{1}$0] crystal directions, respectively. Periodic boundary conditions were applied in all directions. The final ordered structure was further refined by adjusting the composition to form the $D0_{19}$ superlattice structure, as shown in Fig. 3 of the main text. All simulations were carried out using the LAMMPS package[84] (version lammps-2Aug2023), and the atomic configurations were visualized with the Ovito package[85].

SFE calculation

GSFEs, or γ surfaces, were evaluated using the EAM potential, which involved over 100,000 atoms for each calculation. During the GSFE calculations, half of the crystal was displaced by a designated vector, and the structure was allowed to relax in the direction perpendicular to the SF planes.

Formation energies of certain SFs (i.e., SFEs) in the fcc and $D0_{19}$ phases (see, e.g., Supplementary Table 5) were further accurately evaluated following ab initio methods. To this end, various types of SFs were created for the fcc and $D0_{19}$ phases. For instance, the SFs on the basal plane of the $D0_{19}$ phase are illustrated in Supplementary Fig. 13. We used a slab method for the SFE calculation, typically involving more than 300 atoms per configuration. Energy minimization was carried out to obtain structurally relaxed configurations in all directions. Due to the random occupancies of some atoms in both structures, we typically averaged over 20 configurations for each type of SF in our DFT treatment.

Minimum energy path (MEP) calculation

Atomic plane slip occurs along an MEP, revealing the energy barriers and slip directions. In this work, the MEP for a given slip system was determined using the nudged elastic band (NEB) method[86] with both DFT and EAM treatments. In MEP calculations, the slip direction is

often referred to as the reaction coordinate. The initial configuration represents a perfect crystal, while the final configuration corresponds to a crystal with one-half shifted by a Burgers vector. For instance, in the case of pyramidal I slip, it occurs along the <11$\bar{2}$6> direction on the {2$\bar{2}$01} plane. The initial configuration typically consists of more than 300 atoms, arranged so that the slip plane is perpendicular to the z direction. The configuration was structured in a slab mode with periodic boundary conditions applied to the x and y directions only. In our NEB calculations, the bottom two layers of atoms in the z direction were kept fixed to prevent motion of the bottom part. We typically used 16 images along the slip direction for the NEB calculations. For systems involving a very large Burgers vector, such as <11$\bar{2}$6 >/3 in the pyramidal I slip (which is roughly 9.8 Å in length), the NEB calculation was performed in two steps due to the extensive computational requirements of the DFT treatment. The first NEB run solved for the MEP toward the intermediate antiphase boundary (APB) configuration, located in the middle of the large Burgers vector, and the second step solved for the MEP from the APB configuration to the final configuration.

CRSS calculation

For each slip system, the CRSS was determined as the minimum stress that activates the motion of the dislocation on the slip system, using classical MD. We considered the motion of edge dislocations in five different slip systems for the fcc and $D0_{19}$ phases of Ni–Co–Cr–V (as listed in Supplementary Table 6). Edge dislocations for each slip system were created by superposing two half-crystals, followed by structural relaxations[87]. This method is found to be more effective than alternative approaches[88] in creating stable superdislocations due to the large Burgers vector involved. The dimensions and the number of atoms in the simulation system are provided in Supplementary Table 6.

For dislocation activation simulations, the slip plane was placed on the xy-plane, perpendicular to the z direction, as shown in Fig. 7 and Supplementary Figs. 13 and 14. During our MD simulations, periodic boundary conditions were applied in the x and y directions only, with surfaces along the z direction. Stress was applied to the crystal by adding unilateral forces to the atoms on the outer layers (with a thickness of 1 nm) parallel to the slip plane (i.e., along the x direction). The total momentum was zeroed out during the simulation. We used a bisection method to determine the minimum stress that drives the (super)dislocation to sweep through the crystal within 500 ps. Our MD simulations were carried out in NVT ensembles, with a timestep of 2 fs at 298 K. The MD trajectories and scripts for calculating the CRSS are provided in the Supplementary Data.

Statistics and reproducibility

All experiments were repeated independently with similar results multiple times. To elucidate the microstructural characteristics of the fcc/$D0_{19}$ dual-phase UFG architecture in the CR750 alloy, SAED patterns were systematically acquired along multiple zone axes, including [0001], [11$\bar{2}$0], and [10$\bar{1}$0]. These diffraction analyses were complemented by corresponding low-magnification STEM-BF images and atomic-resolution STEM-HAADF imaging to provide comprehensive structural characterization at different length scales. For comprehensive microstructural characterization, multiple low-magnification STEM-BF images (>10 images per observation direction) were systematically acquired. Additionally, an extensive set of atomic-resolution STEM-HAADF images (>20 images) was obtained along the [11$\bar{2}$0] zone axis to reveal detailed atomic arrangements.

Data availability

All relevant data are available from the authors, and/or are included within the manuscript and Supplementary Information. The EAM

potential developed for the Ni–Co–Cr–V system is provided in the Supplementary Data. Source data are provided with this paper.

Code availability

The EAM potential is provided in the Supplementary Data.

References

1. Wei, Y. et al. Evading the strength-ductility trade-off dilemma in steel through gradient hierarchical nanotwins. *Nat. Commun.* **5**, 3580 (2014).
2. Li, Z., Pradeep, K. G., Deng, Y., Raabe, D. & Tasan, C. C. Metastable high-entropy dual-phase alloys overcome the strength-ductility trade-off. *Nature* **534**, 227–230 (2016).
3. He, B. B. et al. High dislocation density-induced large ductility in deformed and partitioned steels. *Science* **357**, 1029–1032 (2017).
4. Li, Y., et al. Ductile 2-GPa steels with hierarchical substructure. *Science* **379**, 168–173 (2023).
5. Spaeder, G. J. Impact transition behavior of high-purity l8Ni maraging steel. *Metall. Mater. Trans.* **1**, 2011–2014 (1970).
6. Liu, D. et al. Exceptional fracture toughness of CrCoNi-based medium- and high-entropy alloys at 20 Kelvin. *Science* **378**, 978–983 (2022).
7. Pan, Q. et al. Atomic faulting induced exceptional cryogenic strain hardening in gradient cell structured alloy. *Science* **382**, 185–190 (2023).
8. Ma, E. & Wu, X. Tailoring heterogeneities in high-entropy alloys to promote strength-ductility synergy. *Nat. Commun.* **10**, 5623 (2019).
9. Ding, Q. et al. Tuning element distribution, structure and properties by composition in high entropy alloys. *Nature* **574**, 223–227 (2019).
10. Li, Q. J., Sheng, H. & Ma, E. Strengthening in multi-principal element alloys with local-chemical-order roughened dislocation pathways. *Nat. Commun.* **10**, 3563 (2019).
11. Sohn, S. S. et al. Ultrastrong medium-entropy single-phase alloys designed via severe lattice distortion. *Adv. Mater.* **31**, 1807142 (2019).
12. Yang, T. et al. Ductilizing brittle high-entropy alloys via tailoring valence electron concentrations of precipitates by controlled elemental partitioning. *Mater. Res. Lett.* **6**, 600–606 (2018).
13. Shi, P. et al. Enhanced strength-ductility synergy in ultrafine-grained eutectic high-entropy alloys by inheriting microstructural lamellae. *Nat. Commun.* **10**, 489 (2019).
14. Shi, P. et al. Multistage work hardening assisted by multi-type twinning in ultrafine-grained heterostructural eutectic high-entropy alloys. *Mater. Today* **41**, 62–71 (2020).
15. Tong, Y. et al. Outstanding tensile properties of a precipitation-strengthened FeCoNiCrTi$_{0.2}$ high-entropy alloy at room and cryogenic temperatures. *Acta Mater.* **165**, 228–240 (2019).
16. Fan, L. et al. Ultrahigh strength and ductility in newly developed materials with coherent nanolamellar architectures. *Nat. Commun.* **11**, 6240 (2020).
17. Zhang, C. et al. Strong and ductile FeNiCoAl-based high-entropy alloys for cryogenic to elevated temperature multifunctional applications. *Acta Mater.* **242**, 118449 (2023).
18. Sathiyamoorthi, P. et al. Exceptional cryogenic strength-ductility synergy in Al$_{0.3}$CoCrNi medium entropy alloy through heterogeneous grain structure and nano-scale precipitates. *Mater. Sci. Eng. A* **766**, 138372 (2019).
19. Bhattacharjee, T. et al. Effect of low temperature on tensile properties of AlCoCrFeNi$_{2.1}$ eutectic high entropy alloy. *Mater. Chem. Phys.* **210**, 207–212 (2018).
20. Chen, G. et al. Polysynthetic twinned TiAl single crystals for high-temperature applications. *Nat. Mater.* **15**, 876–881 (2016).
21. Carvalho, P. A., Bronsveld, P. M., Kooi, B. J. & De Hosson, J. T. M. On the fcc → DO$_{19}$ transformation in Co–W alloys. *Acta Mater.* **50**, 4511–4526 (2002).
22. Hagihara, K., Nakano, T. & Umakoshi, Y. Plastic deformation behavior of oriented Ni$_3$Sn crystals with DO$_{19}$ structure. *Scr. Mater.* **48**, 577–581 (2003).
23. Song, L. et al. Evidence for deformation twinning of the DO$_{19}$-α_2 phase in a high Nb containing TiAl alloy. *Intermetallics* **109**, 91–96 (2019).
24. Song, L. et al. New insights into high-temperature deformation and phase transformation mechanisms of lamellar structures in high Nb-containing TiAl alloys. *Acta Mater.* **186**, 575–586 (2020).
25. Sun, S. J. et al. Temperature dependence of the Hall-Petch relationship in CoCrFeMnNi high-entropy alloy. *J. Alloys Compd.* **806**, 992–998 (2019).
26. Tirunilai, A. S. et al. Comparison of cryogenic deformation of the concentrated solid solutions CoCrFeMnNi, CoCrNi and CoNi. *Mater. Sci. Eng. A* **783**, 139290 (2020).
27. Pu, Z. et al. Spatio-temporal dynamics of jerky flow in high-entropy alloy at extremely low temperature. *Philos. Mag.* **101**, 154–178 (2021).
28. Gan, B. et al. Superb cryogenic strength of equiatomic CrCoNi derived from gradient hierarchical microstructure. *J. Mater. Sci. Technol.* **35**, 957–961 (2019).
29. Liu, X. et al. Mechanical property comparisons between CrCoNi medium-entropy alloy and 316 stainless steels. *J. Mater. Sci. Technol.* **108**, 256–269 (2022).
30. Yang, M. et al. High impact toughness of CrCoNi medium-entropy alloy at liquid-helium temperature. *Scr. Mater.* **172**, 66–71 (2019).
31. Yang, D. C., Jo, Y. H., Ikeda, Y., Körmann, F. & Sohn, S. S. Effects of cryogenic temperature on tensile and impact properties in a medium-entropy VCoNi alloy. *J. Mater. Sci. Technol.* **90**, 159–167 (2021).
32. Nutor, R. K. et al. Liquid helium temperature deformation and local atomic structure of CoNiV medium entropy alloy. *Mater. Today Commun.* **30**, 103141 (2022).
33. Sun, L. et al. Local chemical order enables an ultrastrong and ductile high-entropy alloy in a cryogenic environment. *Sci. Adv.* **10**, eadq6398 (2024).
34. Gao, X. et al. Excellent strength-ductility combination of Cr$_{26}$Mn$_{20}$Fe$_{20}$Co$_{20}$Ni$_{14}$ high-entropy alloy at cryogenic temperatures. *J. Mater. Sci. Technol.* **154**, 166–177 (2023).
35. Ming, K. et al. Dynamically reversible shear transformations in a CrMnFeCoNi high-entropy alloy at cryogenic temperature. *Acta Mater.* **232**, 117937 (2022).
36. Liu, J. et al. Excellent ductility and serration feature of metastable CoCrFeNi high-entropy alloy at extremely low temperatures. *Sci. China Mater.* **62**, 853–863 (2019).
37. Wang, S. et al. Mechanical instability and tensile properties of TiZrHfNbTa high entropy alloy at cryogenic temperatures. *Acta Mater.* **201**, 517–527 (2020).
38. Kim, D. G. et al. Ultrastrong duplex high-entropy alloy with 2 GPa cryogenic strength enabled by an accelerated martensitic transformation. *Scr. Mater.* **171**, 67–72 (2019).
39. Li, D., Li, Z., Xie, L., Zhang, Y. & Wang, W. Cryogenic mechanical behavior of a TRIP-assisted dual-phase high entropy alloy. *Nano Res* **15**, 4859–4866 (2022).
40. Wang, Z., Lu, W., Raabe, D. & Li, Z. On the mechanism of extraordinary strain hardening in an interstitial high-entropy alloy under cryogenic conditions. *J. Alloys Compd.* **781**, 734–743 (2019).
41. Bae, J. W. et al. Exceptional phase-transformation strengthening of ferrous medium-entropy alloys at cryogenic temperatures. *Acta Mater.* **161**, 388–399 (2018).
42. Zuo, Y. et al. Cryogenic deformation strengthening mechanisms in FeMnSiNiAl high-entropy alloys. *Acta Mater.* **283**, 120554 (2025).

43. Zhang, D. D., Zhang, J. Y., Kuang, J., Liu, G. & Sun, J. The B2 phase-driven microstructural heterogeneities and twinning enable ultra-high cryogenic strength and large ductility in NiCoCr-based medium-entropy alloy. *Acta Mater.* **233**, 117981 (2022).

44. Kumar, P. et al. A strong fracture-resistant high-entropy alloy with nano-bridged honeycomb microstructure intrinsically toughened by 3D-printing. *Nat. Commun.* **15**, 841 (2024).

45. Górecki, K., Bała, P., Bednarczyk, W. & Kawałko, J. Cryogenic behaviour of the $Al_5Ti_5Co_{35}Ni_{35}Fe_{20}$ multi-principal component alloy. *Mater. Sci. Eng. A* **745**, 346–352 (2019).

46. Sohail, Y. et al. A complex concentrated alloy with record-high strength-toughness at 77 K. *Adv. Mater.* **37**, 2410923 (2025).

47. Zhou, Y. H. et al. A strong-yet-ductile high-entropy alloy in a broad temperature range from cryogenic to elevated temperatures. *Acta Mater.* **268**, 119770 (2024).

48. Li, W. et al. Design of ultrastrong but ductile medium-entropy alloy with controlled precipitations and heterogeneous grain structures. *Appl. Mater. Today* **23**, 101037 (2021).

49. Wang, F. et al. Shearing brittle intermetallics enhances cryogenic strength and ductility of steels. *Science* **384**, 1017–1022 (2024).

50. Li, C., Li, K., Dong, J., Wang, J. & Shao, Z. Mechanical behavior and microstructure of Fe-20/27Mn-4Al-0.3C low magnetic steel at room and cryogenic temperatures. *Mater. Sci. Eng. A* **809**, 140998 (2021).

51. Luo, Q. et al. On mechanical properties of novel high-Mn cryogenic steel in terms of SFE and microstructural evolution. *Mater. Sci. Eng. A* **753**, 91–98 (2019).

52. Ren, J. et al. Fe–Mn–Al–C high-entropy steels with superior mechanical properties at 4.2. *K. Mater. Des.* **228**, 111840 (2023).

53. Zheng, C. & Yu, W. Effect of low-temperature on mechanical behavior for an AISI 304 austenitic stainless steel. *Mater. Sci. Eng. A* **710**, 359–365 (2018).

54. Moon, J. et al. Deformation behavior of a Co–Cr–Fe–Ni–Mo medium-entropy alloy at extremely low temperatures. *Mater. Today* **50**, 55–68 (2021).

55. Zhou, X. et al. Superior tensile properties and unique damage-fracture characteristics of Ti-2.5Cu α-titanium alloy at liquid-nitrogen temperature. *J. Alloys Compd.* **967**, 171753 (2023).

56. Zang, M. C., Niu, H. Z., Zhang, H. R., Tan, H. & Zhang, D. L. Cryogenic tensile properties and deformation behavior of a superhigh strength metastable beta titanium alloy Ti-15Mo-2. *Al. Mater. Sci. Eng. A* **817**, 141344 (2021).

57. Zang, M. C. et al. Achieving high tensile strength-ductility synergy of a fully-lamellar structured near alpha titanium alloy at extra-low temperatures. *J. Alloys Compd.* **923**, 166363 (2022).

58. Niu, H. Z. et al. Anomalous strain rate dependence of ultra-low temperature strength and ductility of an electron beam additively manufactured near alpha titanium alloy. *J. Mater. Sci. Technol.* **198**, 44–55 (2024).

59. Zang, M. C. et al. Achieving highly promising strength-ductility synergy of powder bed fusion additively manufactured titanium alloy components at ultra-low temperatures. *Addit. Manuf.* **65**, 103444 (2023).

60. Semenova, I. P. et al. Fracture toughness at cryogenic temperatures of ultrafine-grained Ti-6Al-4V alloy processed by ECAP. *Mater. Sci. Eng. A* **716**, 260–267 (2018).

61. Wang, H., Sun, Q. Y., Xiao, L. & Sun, J. Effect of grain size on twinning behavior in Ti-2Al-2.5Zr alloy fatigued at 77. *K. Mater. Sci. Eng. A* **542**, 1–7 (2012).

62. Kim, S. H., Hong, S. I. & Kim, S. J. On the rule of mixtures for predicting the mechanical properties of composites with homogeneously distributed soft and hard particles. *J. Mater. Process. Technol.* **112**, 109–113 (2001).

63. Bu, Y. et al. Nonbasal slip systems enable a strong and ductile hexagonal-close packed high entropy phase. *Phys. Rev. Lett.* **122**, 075502 (2019).

64. Naeem, M. et al. Cooperative deformation in high-entropy alloys at ultralow temperatures. *Sci. Adv.* **6**, eaax4002 (2020).

65. De Cooman, B. C., Estrin, Y. & Kim, S. K. Twinning-induced plasticity (TWIP) steels. *Acta Mater.* **142**, 283–362 (2018).

66. Jo, Y. H. et al. Cryogenic strength improvement by utilizing room-temperature deformation twinning in a partially recrystallized VCrMnFeCoNi high-entropy alloy. *Nat. Commun.* **8**, 15719 (2017).

67. Su, R. et al. Ultra-high strength and plasticity mediated by partial dislocations and defect networks: Part I: Texture effect. *Acta Mater.* **185**, 181–192 (2020).

68. Ma, Y. et al. Dynamic shear deformation of a CrCoNi medium-entropy alloy with heterogeneous grain structures. *Acta Mater.* **148**, 407–418 (2018).

69. Laplanche, G. et al. Reasons for the superior mechanical properties of medium-entropy CrCoNi compared to high-entropy CrMnFeCoNi. *Acta Mater.* **128**, 292–303 (2017).

70. Cockayne, D. J. H. The principles and practice of the weak-beam method of electron microscopy. *J. Microsc.* **98**, 116–134 (1973).

71. Chung, H. et al. Effect of solid-solution strengthening on deformation mechanisms and strain hardening in medium-entropy $V_{1-\chi}Cr_\chi CoNi$ alloys. *J. Mater. Sci. Technol.* **108**, 270–280 (2022).

72. Harjo, S. et al. Current status of engineering materials diffractometer at J-PARC. *Mater. Sci. Forum* **681**, 443–448 (2011).

73. Jin, X. et al. Development of a cryogenic load frame for the neutron diffractometer at Takumi in Japan Proton Accelerator Research Complex. *Rev. Sci. Instrum.* **84**, 063106 (2013).

74. Wei, D. et al. Metalloid substitution elevates simultaneously the strength and ductility of face-centered-cubic high-entropy alloys. *Acta Mater.* **225**, 117571 (2022).

75. Wei, D. et al. Si-addition contributes to overcoming the strength-ductility trade-off in high-entropy alloys. *Int. J. Plast.* **159**, 103443 (2022).

76. Sarkar, A., Mukherjee, P. & Barat, P. X-ray diffraction studies on asymmetrically broadened peaks of heavily deformed zirconium-based alloys. *Mater. Sci. Eng. A* **485**, 176–181 (2008).

77. Donkor, B. T. et al. Accelerated γ-face-centered cubic to ε-hexagonal close packed massive transformation in a laser powder bed fusion additively manufactured Co-29Cr-5Mo alloy. *Scr. Mater.* **179**, 65–69 (2020).

78. Blöchl, P. E. Projector augmented-wave method. *Phys. Rev. B* **50**, 17953–17979 (1994).

79. Kresse, G. & Joubert, D. From ultrasoft pseudopotentials to the projector augmented-wave method. *Phys. Rev. B* **59**, 1758–1775 (1999).

80. Daw, M. S. & Baskes, M. I. Embedded-atom method: derivation and application to impurities, surfaces, and other defects in metals. *Phys. Rev. B* **29**, 6443–6453 (1984).

81. Brommer, P. & Gähler, F. Potfit: effective potentials from ab initio data. *Model. Simul. Mater. Sci. Eng.* **15**, 295 (2007).

82. Cheng, Y. Q., Ma, E. & Sheng, H. W. Atomic level structure in multicomponent bulk metallic glass. *Phys. Rev. Lett.* **102**, 245501 (2009).

83. Sadigh, B. et al. Scalable parallel Monte Carlo algorithm for atomistic simulations of precipitation in alloys. *Phys. Rev. B* **85**, 184203 (2012).

84. Plimpton, S. Fast parallel algorithms for short-range molecular dynamics. *J. Comput. Phys.* **117**, 1–19 (1995).

85. Stukowski, A. Visualization and analysis of atomistic simulation data with OVITO—the open visualization tool. *Model. Simul. Mater. Sci. Eng.* **18**, 15012 (2010).

86. Jónsson, H., Mills, G. & Jacobsen, K. W. *Classical and Quantum Dynamics in Condensed Phase Simulations* (eds Berne, B. J. et al.) Ch. 385 (World Scientific Publ. Co, 1998).

87.   Osetsky, Y. N. & Bacon, D. J. An atomic-level model for studying the dynamics of edge dislocations in metals. *Model. Simul. Mater. Sci. Eng.* **11**, 427 (2003).
88.   Hirel, P. Atomsk: A tool for manipulating and converting atomic data files. *Comput. Phys. Commun.* **197**, 212–219 (2015).
89.   Qi, J. et al. Machine learning moment tensor potential for modeling dislocation and fracture in $L1_0$-TiAl and DO_{19}-Ti_3Al alloys. *Phys. Rev. Mater.* **7**, 103602 (2023).

Acknowledgements

Author contributions

G.C. proposed and supervised the project. Z.C. performed most of the properties and the structural characterizations. D.W., W.G., S.H. and T.K. measured the in situ neutron diffraction experiments. H.S. performed the theoretical calculations. Z.C., Y.C., H.S., D.W. and G.C. analyzed the data. Xu L., Xuan L., H.X., R.H., J.Z., D.Z., G.Z. and Z.Q. contributed to the result discussion. J.T., L.L. and J.X. assisted with the sample preparation. Z.C., Y.C., H.S. and G.C. conceptualized the manuscript. The final version was approved by all authors before submission.

Competing interests

The authors declare no competing interests.

Additional information

Supplementary information The online version contains supplementary material available at https://doi.org/10.1038/s41467-025-61494-7.

Correspondence and requests for materials should be addressed to Howard Sheng or Guang Chen.

Peer review information *Nature Communications* thanks the anonymous reviewers for their contribution to the peer review of this work. A peer review file is available.

Reprints and permissions information is available at http://www.nature.com/reprints

Publisher's note Springer Nature remains neutral with regard to jurisdictional claims in published maps and institutional affiliations.